



Contents lists available at ScienceDirect

Journal of the Mechanics and Physics of Solids

journal homepage: www.elsevier.com/locate/jmps

Effect of elasticity on phase separation in heterogeneous systems

Mrityunjay Kothari^a, Tal Cohen^{a,b,*}^a Department of Civil and Environmental Engineering, Massachusetts Institute of Technology, Cambridge, 02139 MA, USA^b Department of Mechanical Engineering, Massachusetts Institute of Technology, Cambridge, MA, 02139 USA

ARTICLE INFO

Article history:

Received 28 May 2020

Revised 29 July 2020

Accepted 6 September 2020

Available online 19 September 2020

Keywords:

Liquid-liquid phase separation

Ostwald ripening

Elasticity

Front propagation

ABSTRACT

Physical systems consisting of an elastic matrix permeated by fluid mixture are ubiquitous, with examples ranging from morphogenesis of a single biological cell to the migration of greenhouse gases in sediments. Recent experimental studies show that the presence of the elastic networks in these systems significantly alters their phase-separation response by imposing an energetic cost to the growth of droplets. However, a quantitative understanding of the role played by elasticity is lacking. Our paper bridges this gap by building a comprehensive theoretical framework to analyze the effect of elasticity on the phase separation of a binary mixture in soft, nonlinear solids. We employ an energy-based approach that captures both the short-time quasi-equilibrium and the long-time evolution of the phase separation, in elastically homogeneous as well as heterogeneous materials, to determine the constitutive sensitivities. Our theory predicts a droplet dissolution front in heterogeneous materials. Crucially, we also find a nonlinear effect of elasticity on the dynamics, which challenges the current understanding in the literature. We quantify the thermodynamic driving forces to identify diffusion-limited and dissolution-limited regimes of front propagation. Our findings are applicable to a variety of material systems including food, metals, and aquatic sediments, and further substantiate the hypothesis that biological systems exploit such mechanisms to regulate their function.

© 2020 Published by Elsevier Ltd.

1. Introduction

Phase separation is observed across scales and in a variety of physical processes that range from the fields of biology to metallurgy. Liquid-liquid phase separation and subsequent species migration is understood to be a crucial mechanism for regulating the normal bodily functions of a cell. For instance, P-granule assembly is believed to employ phase separation as a mechanism to polarize the cell along its anterior-posterior axis as a precursor to cell differentiation (Brangwynne et al., 2009; Lee et al., 2013; Saha et al., 2016; Weber et al., 2017; 2019). The dynamics of this process is dependent on the cytoplasm and its mechanical properties. In metals, phase transitions are extensively employed to tailor the mechanical properties for a variety of applications ranging from cryogenic temperature applications (Kothari et al., 2019) such as LNG transport to high temperature applications like furnaces (Smith et al., 2016; Tancret et al., 2018). The morphology and distribution of precipitates resulting from phase transition in metals is also affected by the presence of elastic fields (Doi et al., 1985; Fratzl et al., 1999; Karpov, 1998; Nabarro, 1940). This effect is of particular importance in the food industry,

* Corresponding author at: Department of Civil and Environmental Engineering, Massachusetts Institute of Technology, Cambridge, 02139 MA, USA.
E-mail address: talco@mit.edu (T. Cohen).

where phase separation controls how different components of the food interact, resulting in the texture and the flavor of the dish. The stable distribution of particles of one phase in another, such as water-in-oil in salad dressing, ice-in-cream in ice cream and air-in-protein network in bread not only impacts its flavor but also its longevity. Elasticity is also believed to play an important role in determining the size of gas bubbles that are formed in sediments, and their ability to migrate. For example, the growth of methane bubbles in aquatic sediments, and the subsequent transport of this potent greenhouse gas to the atmosphere can be significantly affected by the heterogeneous elastic properties of the surrounding medium (Algar and Boudreau, 2010; Johnson et al., 2002; Liu et al., 2018).

From these examples spanning various fields, we see that elasticity emerges as a common denominator that has a significant bearing on the final outcome of phase separation. Elasticity provides a way to not only deepen our understanding of biological principles of organisation but also to improve existing technologies to better control material microstructure and to improve the stability and shelf life of food. While important work has been carried out, both experimentally and theoretically, in understanding the elastic effects on phase separation and species migration in soft-material systems, a complete theoretical understanding of the dynamics of these processes still presents many challenges. In practical applications, the matrix properties are often heterogeneous, and the phase separation process is sensitive to these non-uniformities. Additionally, phase separation can induce large deformations in the elastic matrix, thus giving rise to nonlinear material response, which can lead to distinct phase separation behavior even among materials with similar properties at the linear elastic limit. Furthermore, the connection between elasticity and the timescales associated with the phase separation is not well understood. In this work, we overcome these challenges to obtain a quantitative understanding of the role of elasticity in the short and long-time dynamics of phase separation.

The interruption of phase separation due to the elastic resistance of a cross-linked network was first theoretically predicted by de Gennes (1979) and termed as *microphase separation*. Subsequent experiments by Briber and Bauer (1988) confirmed this microphase separation by considering the nucleation behavior in deuteriated polystyrene (PSD) and poly(vinyl methyl ether) (PVME), although the results showed deviation from the predicted trends. Recent works (Rosowski et al., 2020a; Style et al., 2018; Vidal-Henriquez and Zwicker, 2020) have studied phase separation in a quenched mixture of liquid polydimethylsiloxane (PDMS) and fluorinated oil in crosslinked PDMS. The minority component (fluorinated oil) separated into nearly-monodisperse spherical droplets, spread throughout the crosslinked PDMS. It was reported that the stiffness of the polymer controls the size of the droplets and the nucleation temperature. However, the theoretical underpinnings of how elasticity controls the nucleation temperature, selects a particular equilibrium droplet size and can lead to the migration of species across stiffness gradients remain to be quantitatively understood.

There are two important timescales in the phase separation response of a liquid mixture in presence of elastic effects. At the short timescale, a rapid quench leads to the nucleation of liquid droplets of the dilute phase in the matrix. The droplets grow to a stable size dictated by the local elastic properties of the matrix. Any spatial heterogeneities in the stiffness of the matrix result in non-uniform solubility of the dilute phase. At the long timescale, these non-uniformities in the matrix concentration set up a diffusive flux in the matrix which alters the droplet sizes and can create a propagating front of dissolving droplets. In this paper, we first develop a theory to model the quasi-equilibrium phase separation response at the short timescale. This sets up the groundwork for modeling the long-time kinetics in spatially heterogeneous material systems and leads to a quantitative understanding of how elasticity controls the speed of the front. To validate our theory, we compare the predictions of our model with experimental results in the literature. In particular, we explain through our model the observation of a propagating droplet dissolution front in a composite elastic sample made of stiff and soft materials (Rosowski et al., 2020a).

2. Theory of phase separation with elastic effects

2.1. Problem setting and governing equations

Our model system consists of a partially cross-linked polymer with liquid *A* that is soaked in a bath of liquid *B* at temperature T_1 . At equilibrium, this results in the polymer being saturated with a small volume fraction of liquid *B*, denoted by $\phi_{sat}(T_1)$. This assembly is taken out of the bath and rapidly quenched to a lower temperature T (Fig. 1) where the mixture becomes unstable and demixes, giving rise to droplets of liquid *B*. We distinguish between two phases in our system; the droplets, which contain only liquid *B*, and the ‘matrix’ that is occupied by the crosslinked network and permeated by liquids *A* and *B*.

For a mathematical description of the system we introduce the following notations: $\phi_A = V_A/V_M$ and $\phi_B = V_B/V_M$ denote the volume fractions of liquids *A* and *B* in the matrix, where V_M denotes the volume of the matrix within a representative unit element of the material system, and V_A , V_B are the separate volumes of liquids *A* and *B* within the matrix, respectively. The total volume of the unit is $V = V_M + V_D$, where V_D is the total volume of droplets. The volume fraction of droplets is $\phi_D = V_D/V$. The initial volume of polymer within the unit element (without liquid *B*) can be written as $V_0 = (1 - \phi_B)V_M$, and the volume fractions of the two liquids are related by

$$\phi_A = \frac{V_A}{V_0}(1 - \phi_B). \quad (1)$$

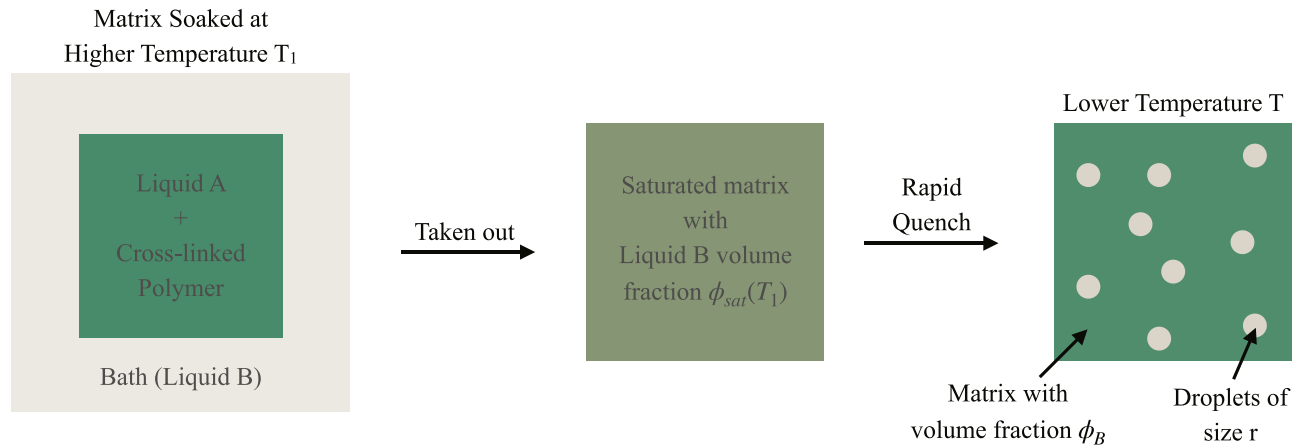


Fig. 1. Schematic of the phase separation process. The matrix material made of liquid A and crosslinked polymer, is soaked in a bath of liquid B at an elevated temperature and saturated with a volume fraction $\phi_{sat}(T_1)$ of liquid B. Then, this assembly is quenched rapidly. The mixture phase separates into two components - (1) matrix consisting of crosslinked polymer and liquids A and B, and (2) droplets of liquid B. The size of droplets and the volume fractions are controlled by elasticity.

We make the following assumptions in our model. We consider the model in the thermodynamic size limit so that there are no effects due to the finiteness of the system. Liquid B is the minority phase and has a small volume fraction ($\phi_B \ll 1$). Liquid B is the only mobile component in the system; both V_A and V_0 remain constant throughout the process. We consider situations in which the matrix does not swell appreciably in the entire process, and thus changes in elastic energy due to the swelling of the matrix can be neglected. Accordingly, we model the process as mixing between two liquids A and B , with the cross-linked network only providing elastic resistance to droplet growth. Further, motivated by a recent experimental study (Style et al., 2018), we will take the droplet size distribution to be monodisperse, hence we write

$$\phi_D \equiv \frac{4\pi}{3} r^3 n_d, \quad (2)$$

where r denotes the radius of the droplets, and n_d denotes their number density. We assume that the number density is determined by the initial kinetics of phase separation. Hence, we do not attempt to model these kinetics in this paper; guided by (Style et al., 2018) we choose a linear dependence of n_d on the matrix stiffness.

The change in total free energy density of the system, calculated per unit volume, can be expressed as the sum of contributions from mixing ($\Delta\bar{G}_{mix}$), elastic ($\Delta\bar{G}_{el}$) and surface energies ($\Delta\bar{G}_{sur}$) as,

$$\Delta\bar{G}(\phi_A, \phi_B, \phi_D, T) = \Delta\bar{G}_{mix}(\phi_A, \phi_B, T) + \Delta\bar{G}_{sur}(\phi_D) + \Delta\bar{G}_{el}(\phi_D), \quad (3)$$

$$\Delta\bar{G}_{el}(\phi_D) = \frac{4\pi}{3} r^3 W(r) n_d, \quad (4)$$

$$\Delta\bar{G}_{sur}(\phi_D) = 4\pi r^2 \Gamma n_d, \quad (5)$$

where $W(r)$ is the strain energy density due to a single droplet and Γ is the surface energy between the two liquids. In calculating the total elastic energy in (4), we implicitly assume that the droplets do not elastically interact with each other. This is a reasonable simplification under the small volume fraction assumption ($\phi_B, \phi_D \ll 1$), therefore, we can simply add the elastic energy contribution of all the droplets. Note that the free energy density is written as a function of the volume fractions, such that $\Delta\bar{G} = \Delta\bar{G}(\phi_A, \phi_B, \phi_D, T)$. Using the above definitions, the free energy of a unit element (of volume V) can be written in terms of volumes $\Delta G = \Delta G(V_A, V_B, V_D, T)$. In the derivations to follow, we alternate between these representations for analytical convenience and clarity.

Throughout the quenching and droplet growth process we assume a closed system; sum total of the volume of liquid B dissolved in the matrix and in droplets must be the same as the initial saturation volume of liquid B at T_1 before quenching,

$$\phi_B(1 - \phi_D) + \phi_D = \phi_{sat}(T_1). \quad (6)$$

Eqs. (3)–(6) complete the system of equations to study the effect of elasticity on phase separation.

2.2. Short timescale: elasticity delays phase separation and arrests ostwald ripening

The solubility of liquid B in the matrix typically decreases with temperature (Porter et al., 2009; Rosowski et al., 2020a; Style et al., 2018). As the system is rapidly quenched from initial temperature T_1 , it becomes supersaturated with liquid B .

We define a critical temperature T_c at which a phase-separated state containing r_c sized droplets becomes lower in energy than the homogeneously mixed state. The droplet size r_c can be chosen as the minimum observable size in the experiment, which makes T_c the critical temperature for appearance of *observable* droplets in experiments. Thus, T_c is given as the solution of the following equation,

$$\Delta\bar{G}(\phi_A, \phi_{B,c}, \phi_{D,c}, T) - \Delta\bar{G}(\phi_A, \phi_{sat}(T_1), 0, T) = 0, \quad (7)$$

where from (2) and (6) we have

$$\phi_{D,c} = \frac{4\pi}{3} r_c^3 n_d \quad \text{and} \quad \phi_{B,c} = \frac{\phi_{sat}(T_1) - \phi_{D,c}}{1 - \phi_{D,c}}. \quad (8)$$

After the initial nucleation and growth of droplets, phase-separated liquid mixtures coarsen over time by growing larger droplets at the cost of smaller ones, a process known as *Ostwald Ripening*. The driving force for Ostwald Ripening is the reduction of surface energy. However, elastic networks hinder the coarsening by imposing an energetic cost on larger droplets. As a result, the droplets achieve an equilibrium size that minimizes the total energy of the quenched mixture. Since the total volume of the system remains unchanged during the quenching and growth of droplets, the energy minimization condition for equilibrium can be expressed as,

$$\frac{d\Delta\bar{G}(\phi_A, \phi_B, \phi_D, T)}{d\phi_B} = 0, \quad (9)$$

where ϕ_D and ϕ_B are related by the identity in (6), and the relationship between ϕ_A and ϕ_B is given in (1).

To illustrate the predictions of the model we choose the specific response functions for mixing and elastic free energies. For $\Delta\bar{G}_{mix}$, we use the Flory-Huggins theory:

$$\Delta\bar{G}_{mix}(\phi_A, \phi_B, \phi_D, T) = (1 - \phi_D) \frac{kT}{v_m} \left\{ \frac{\phi_A}{N_A} \ln \phi_A + \phi_B \ln \phi_B + \chi(T) \phi_B (1 - \phi_B) \right\}, \quad (10)$$

where k is the Boltzmann constant, v_m is the molecular volume of liquid B , N_A is the number of lattice sites occupied by a single chain of liquid A and $\chi(T)$ is the Flory interaction parameter. By inserting the free energy density (3), along with relations (4),(5) and (10) into the equilibrium condition (9), we obtain an implicit relation for the equilibrium droplet size,

$$\ln \phi_B + (1 - \phi_B)(1 - 1/N_A) + \chi(1 - \phi_B)^2 = \frac{v_m}{kT} \left(\frac{2\Gamma}{r} + W(r) + \frac{r}{3}W'(r) \right), \quad (11)$$

where ϕ_B is related to the droplet size, r , by the mass conservation constraint (6), along with the identity (2).

Next, we can infer $\chi(T)$ by energy minimization given the knowledge of the saturation volume fraction of liquid B after soaking the matrix in a bath (see Appendix A), to write,

$$\chi = -\frac{\log \phi_{sat} + (1 - \phi_{sat})(1 - 1/N_A)}{(1 - \phi_{sat})^2}. \quad (12)$$

For elastic energy calculations, we choose to model the material as incompressible and use the Mooney-Rivlin constitutive function (Mooney, 1940; Rivlin, 1948) which permits strain-stiffening. The elastic energy density due to a single droplet undergoing expansion from an initial size r_0 to final size r is then given as (see Appendix B for derivation),

$$W(r) = nE \left[\frac{5}{6} - \frac{r_0}{r} - \frac{1}{3} \left(\frac{r_0}{r} \right)^3 + \frac{1}{2} \left(\frac{r_0}{r} \right)^4 \right] + (1 - n)E \left[\frac{r}{2r_0} - \frac{1}{3} - \left(\frac{r_0}{r} \right)^2 \left(\frac{r_0}{r} \right)^3 \right], \quad (13)$$

where E is the stiffness of the crosslinked polymer and $0 \leq n \leq 1$ determines the level of strain stiffening. For $n = 1$, the neo-Hookean material model is recovered as the stiffening effect is eliminated. The neo-Hookean limit has been shown to apply only for moderate strains (Gent, 2001). Additionally, it predicts that the total work done (per unit volume) in expanding a cavity arrives at an asymptotic limit as $r \gg r_0$. Hence, for the neo-Hookean model, expansion of all the cavities will only depend on their total volume and not on their radius. To account for nonlinear strain-stiffening effects that emerge at large strains, the Mooney-Rivlin model (13) includes the second term on the right hand side (with $n < 1$), which restricts the cavity size.

An important parameter that appears in Eq. (13) is the initial cavity size, r_0 , which can be assumed to represent the size of initial defects in the material. For a crosslinked network, it seems natural to choose r_0 as the pore size (i.e. $r_0 \sim 1$ nm). However, in the entire process, starting from nucleation to the growth of the droplet to its final size, there is an inevitable role of inelastic deformations (Kim et al., 2020). Some of these inelastic effects occur while the cavity is still too small for continuum treatment and the thermodynamic forces that drive de-mixing can rupture the network. Additionally, as explained by Gent and Tompkins (1969), at the small-size limit a significant energetic barrier, due to surface energy, hinders the expansion of cavities. Hence, it is expected that, following their nucleation, cavities that appear at weaker spots in the network (such that $r_0 > 1$ nm), are more likely to grow. Further, we argue that for the phenomenon considered in this work, r_0 should be larger than the elastocapillary length scale (Γ/E), since only then the elastic forces will generate appreciable resistance to the growth of cavities. Nonetheless, the precise microscopic mechanisms that drive the nucleation and growth of the initial defects should be subject for future work.

Although the value of r_0 is not known a priori; it can depend on the nucleation kinetics, as does n_d , and may progressively increase with the growth of the droplets; it is possible to estimate a representative value of r_0 from experiments, while the other model parameters (i.e. v_m , ϕ_{sat} , n_d , α , r_c , n , E) can be independently measured. Indeed, we find that a representative value of $r_0 = 0.1 \mu\text{m}$, which obeys the inequality $r_0 \geq \Gamma/E$, within the entire range of considered values of E and Γ , results in a good agreement between the theory and the experimental system considered in Section 3. Henceforth, this effective initial defect size is used to determine the level of circumferential stretch (i.e. $\lambda = r/r_0$) throughout the expansion process at the continuum scale. It should be noted that by considering a constant effective value of r_0 in the entire range, we account only for effects that occur during nucleation and shortly after, while neglecting progressive damage accumulation and its irreversible nature. The consequence of this assumption will be further discussed in Section 3 for an example experimental system, where it will be shown that these effects can be neglected.

In the following, we consider example scenarios to illustrate the results of the model. Fig. 2 shows the short timescale predictions assuming the matrix is initially saturated with liquid B at temperature $T_1 = 40^\circ\text{C}$. The results are obtained using representative values of the model parameters (v_m , ϕ_{sat} , n_d , α , r_c , r_0) to consider the sensitivity of the process to the elastic stiffness E , the surface energy Γ , strain stiffening n , and the supersaturation, which is defined as $\epsilon = \phi_{sat}(T_1)/\phi_{sat}(T) - 1$. While our results do not show any significant sensitivity for $N_A \geq 1$, we assume $N_A \gg 1$ in this paper unless specified otherwise. Lastly, we note that within the range of considered temperatures, thermal effects on the elastic modulus are negligible.

The influence of elasticity and surface energy on the critical temperature for nucleation of droplets with $r_c = 1 \mu\text{m}$ is shown in Fig. 2(a). As observed, a matrix with higher stiffness and higher strain-stiffening requires a deeper quench to undergo phase separation. Surface energy also increases the barrier to the nucleation of droplets. Similar qualitative behaviors are observed for different values of r_c , which can be chosen, for example, as the minimal observable size in an experiment, or the required size in a particular application. Fig. 2(b) shows model predictions for the quasi-equilibrium droplet size of a system that is quenched to $T = 25^\circ\text{C}$. Higher stiffness of the crosslinked polymer leads to a smaller equilibrium droplet size; a similar trend is followed in the strain-stiffening response whereas higher strain-stiffening leads to smaller droplet size. Additionally, it is shown that although surface tension plays an important role in determining the critical temperature

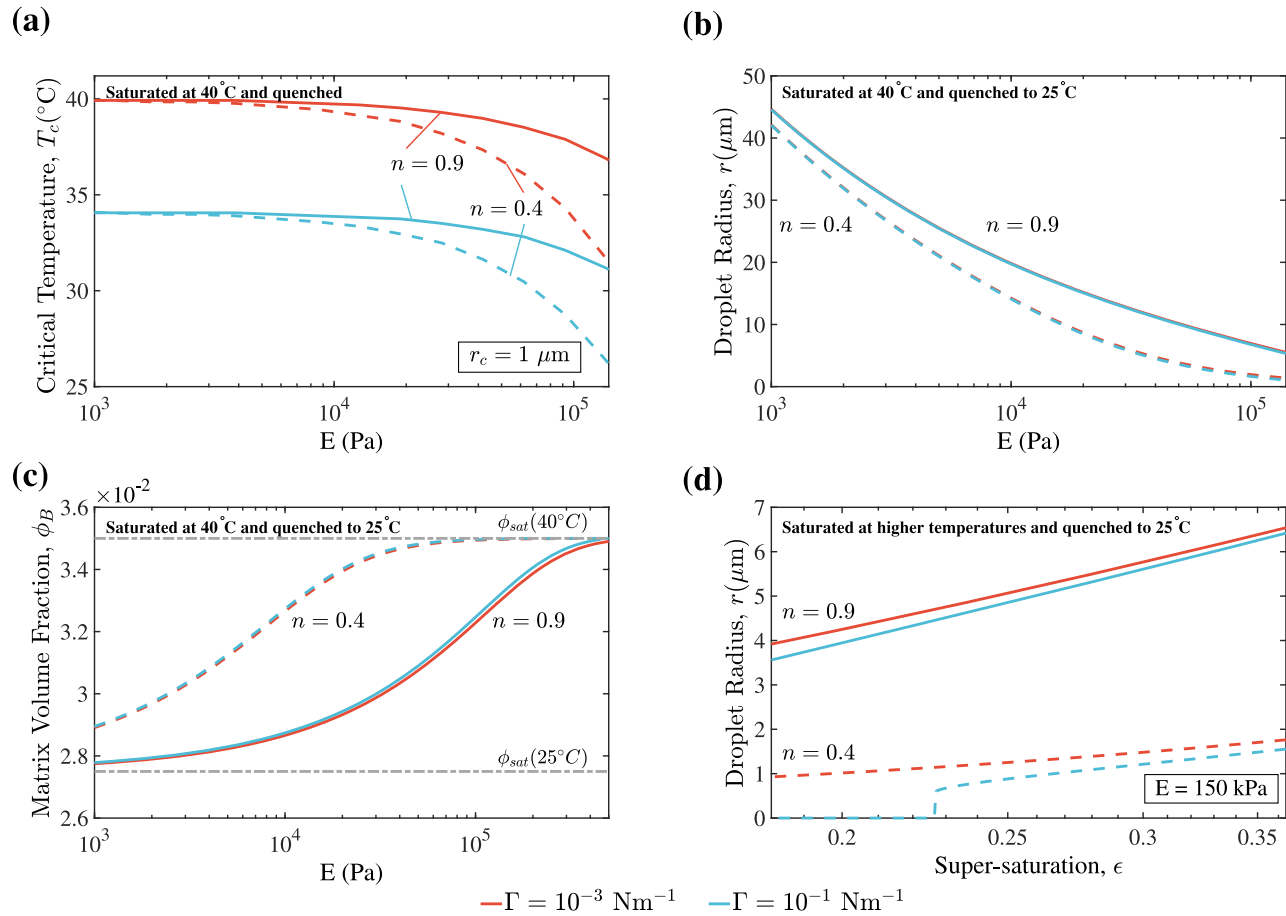


Fig. 2. Elasticity delays phase separation and arrests Ostwald Ripening. Model predictions are obtained for two values of surface tension $\Gamma = 10^{-3}, 10^{-1} \text{ Nm}^{-1}$, and two values of the strain stiffening coefficient $n = 0.4, 0.9$, using the representative model parameters: $v_m = 10^{-27} \text{ m}^3$, $\phi_{sat} = 0.0005T[^\circ\text{C}] + 0.015$, $n_d = \alpha E$, $\alpha = 2 \times 10^7 \text{ N}^{-1} \text{ m}^{-1}$ and $r_0 = 0.1 \mu\text{m}$. Quenching occurs from 40 °C to 25 °C unless noted otherwise. (a) The critical temperature for appearance of droplets of size $r_c = 1 \mu\text{m}$ in a crosslinked polymer, which is initially saturated at 40 °C, as a function of the elastic modulus. It is shown that a deeper quench is required to induce phase separation in a stiffer polymer. Effect of surface tension and strain-stiffening are also noticeable. (b) Quasi-equilibrium droplet size is shown as a function of the elastic stiffness. A modest effect of strain-stiffening is observed while surface tension has a negligible effect. (c) Volume fraction of liquid B in the matrix is shown as a function of the stiffness and reveals an elastic analogue of Gibbs-Thomson effect; higher stiffness leads to higher solubility. (d) The equilibrium size of droplets scales with the supersaturation. Here the system is quenched to 25 °C from different initial temperatures and with $E = 150 \text{ kPa}$.

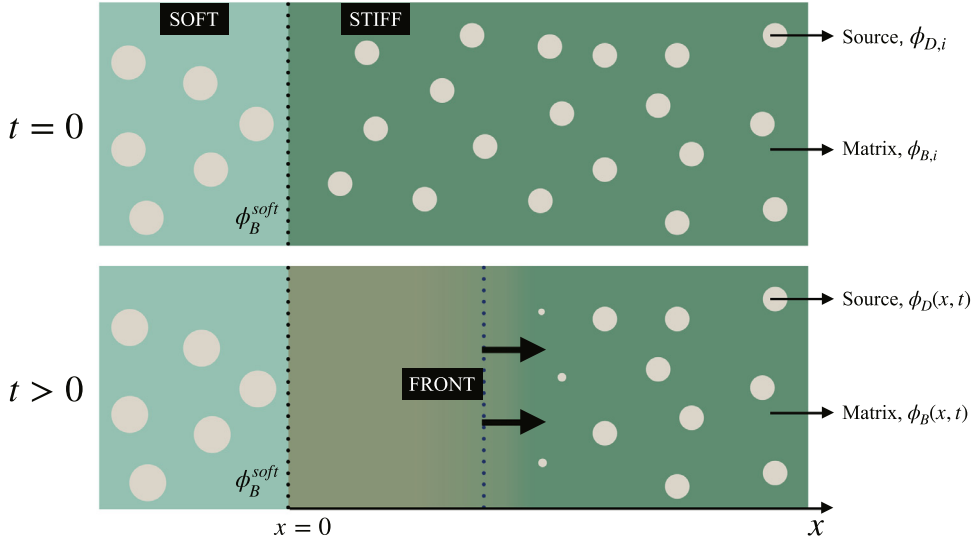


Fig. 3. Schematic of the Front Propagation Process. The graded polymer is made of soft and stiff sides that span indefinitely along the negative and positive directions of the longitudinal coordinate x , respectively. At short timescale ($t = 0$), the system is in the quenched quasi-equilibrium state with droplets distributed throughout. At the long timescale ($t > 0$), the system exhibits long-range migration of liquid B and a resulting closure of droplets.

for appearance of droplets, it does not affect the final droplet size. Fig. 2(c) shows the equilibrium concentration of liquid B in the matrix in the quenched state with 25°C . Analogous to the Gibbs-Thomson effect, elastic stiffness is shown to enhance the solubility of liquid B . Two extremes are observed; in the high stiffness limit, characterized by $Ev_m/\Delta\chi kT \geq 1$ where $\Delta\chi = \chi(T) - \chi(T_1)$, all of the liquid B that was dissolved at T_1 still remains dissolved at the lower temperature T , despite the quench. On the other extreme of low stiffness ($Ev_m/\Delta\chi kT \ll 1$), elasticity leads to negligible enhancement in the solubility and matrix equilibrium concentration becomes $\phi_{\text{sat}}(T)$. In Fig. 2(d) the matrix is saturated at different initial temperatures T_1 and quenched to 25°C to vary the supersaturation, ϵ . As expected, higher supersaturation leads to larger droplet size, while higher stiffness and higher stiffening result in smaller droplets. If the supersaturation is not high enough (or the quench is not deep enough), the droplets may not appear, consistent with Fig. 2(a).

2.3. Long timescale: propagation of dissolution front in graded elastic polymers

In this section, we build on the quasi-equilibrium solution obtained at the short timescale to understand the long-term dynamics of phase separation in spatially heterogeneous materials. Inspired by the experimental work in (Rosowski et al., 2020a), we consider the simplest case of spatial heterogeneity - a uniformly soft and a uniformly stiff polymer joined together (Fig. 3). We assume that quenching is rapid enough so that the short- and long-timescale processes are well separated. As a consequence, the nucleation and growth of droplets to their quasi-equilibrium size is not influenced by the composite nature of the polymer. The droplet distribution on either side is the same as it were in the uniform case (without composite sample), and depends only on the local properties. The short-timescale solution thus serves as the initial condition for the dynamic study. As established earlier, elasticity enhances the solubility, therefore, the stiffer side has higher concentration of liquid B in the matrix as compared to the softer side. This concentration difference between the two sides sets up a diffusive flux of liquid B from higher to lower concentration. As the liquid in the matrix depletes on the stiff side, the droplets serve as a source of liquid B to replenish the matrix. In the analysis, we focus only on the dynamics of the stiff side since that is where we expect the dissolving droplets to create a propagating front. The effect of the soft side is accounted for through the boundary conditions.

We construct a 1-D picture of the above process. The spatial variable is denoted by x ; the soft side, of stiffness E_{soft} , spans $x \in (-\infty, 0)$ and the stiff side, of stiffness E_{stiff} , spans $x \in (0, \infty)$. The matrix and droplet concentrations are now functions of space and time (i.e. $\phi_B = \phi_B(x, t)$ and $\phi_D = \phi_D(x, t)$). Due to the long-range migration of liquid B , the mass conservation constraint (6) no longer holds and $\phi_B(x, t)$ and $\phi_D(x, t)$ are independent variables. We model the droplets as an *exhaustible*, spatially distributed source in the diffusion equation. The dynamical system can be formulated as,

$$\frac{\partial \phi_B}{\partial t} = D \frac{\partial^2 \phi_B}{\partial x^2} + s(\phi_B, \phi_D), \quad (14)$$

$$\frac{\partial \phi_D}{\partial t} = -s(\phi_B, \phi_D), \quad (15)$$

where D is the diffusion constant and $s(\phi_B, \phi_D)$ is the source term. The initial conditions are supplied from the short timescale solution,

$$\phi_B(x > 0, 0) = \phi_{B,i} \quad \text{and} \quad \phi_D(x, 0) = \phi_{D,i}, \quad (16)$$

where $\phi_{B,i}$ is the matrix volume fraction of liquid B at the short-timescale which is in equilibrium with the volume fraction $\phi_{D,i}$ of the droplets. Experiments (Rosowski et al., 2020a) have indicated that liquid B that migrates from the stiff side to the soft side is rapidly taken up by the droplets on the soft side, therefore we assume that the matrix volume fraction on the soft side remains constant over the long timescale. This sets the boundary condition at the $x = 0$ interface; additionally we require that the flux decays at the remote end ($x \rightarrow \infty$), to write the boundary conditions,

$$\phi_B(0, t) = \phi_B^{soft}, \quad (17)$$

$$\frac{\partial \phi_B}{\partial x}(\infty, t) = 0, \quad (18)$$

where ϕ_B^{soft} is the volume fraction of liquid B in the soft side at the short timescale.

The key feature in the above model is the kinetic relation (15), which determines the flow of liquid B from the droplets to the matrix. At the short timescale, the thermodynamic force for phase separation is balanced by the resistance due to elastic and surface energies. When this equilibrium is disturbed by the migration of liquid B in the matrix, the thermodynamic force for phase separation becomes weaker and the droplets start to mix back. This process is controlled by the source term $s(\phi_B, \phi_D)$, which is derived next.

Considering a unit element of the phase separated material system, the local process of expelling fluid from the droplets at rate $\partial V_D/\partial t$, results in the increase of liquid B in the matrix at the rate $\partial V_B/\partial t = -\partial V_D/\partial t$. The corresponding change in free energy must obey the second law of thermodynamics, and thus results in the inequality

$$\frac{\partial \Delta G}{\partial t} = \left(\frac{\partial \Delta G}{\partial V_D} - \frac{\partial \Delta G}{\partial V_B} \right) \frac{\partial V_D}{\partial t} \leq 0, \quad (19)$$

which holds for constant values of V_A and T . Accordingly, we define the *driving force for droplet dissolution*, readily written in terms of volume fractions, as

$$f(\phi_A, \phi_B) = \frac{\partial \Delta G}{\partial V_D} - \frac{\partial \Delta G}{\partial V_B} = \frac{\partial \Delta \bar{G}}{\partial \phi_D} - \left(\frac{1 - \phi_B}{1 - \phi_D} \right) \frac{\partial \Delta \bar{G}}{\partial \phi_B}. \quad (20)$$

This driving force (per unit volume of the material system) serves as the thermodynamic conjugate to the rate of dissolution $\partial V_D/\partial t$, or equivalently, to the rate of change of droplet volume fraction $\partial \phi_D/\partial t$.

In light of the inequality (19), the kinetic relation (15) that governs the rate of dissolution can be chosen as $\partial \phi_D/\partial t = -S(f)$, where the source function $S(f)$ obeys the inequality $fS(f) \geq 0$, for all values of f . While $S(f)$ can take an arbitrary form, the results of this work are obtained using a linear relation $S(f) = Kf$ with the constant kinetic parameter $K > 0$, which applies for small departures from thermodynamic equilibrium. By inserting (3), in (20), this source term further specializes to the form

$$s(\phi_B, \phi_D) = K \left\{ \frac{2\Gamma}{r} + W(r) + \frac{1}{3}W'(r) - \frac{kT}{v_m} \left(\ln \phi_B + (1 - \phi_B)(1 - 1/N_A) + \chi(1 - \phi_B)^2 \right) \right\} H(\phi_D), \quad (21)$$

where $s(\phi_B, \phi_D) = S(f(\phi_B, \phi_D))$ and the Heaviside function $H(\phi_D)$ ensures the source is exhausted when $\phi_D = 0$. Note that, as expected, in the initial state the driving force vanishes, as seen by comparing the above relation with the equilibrium condition (11).

To determine the effect of the kinetic parameter, K , on the dynamics, we return to examine the governing Eqs. (14) and (15). First, it is straight forward to obtain a dimensionless counterpart to K , as

$$\mathcal{K} = \frac{kTL^2K}{Dv_m}, \quad (22)$$

where L is a characteristic length scale of the system. We refer to \mathcal{K} as the *dissolution number*. As observed by comparing the two terms on the right hand side of (14), if $\mathcal{K} \gg 1$ the source is rapidly exhausted and the propagation of the front relies on the diffusion. Hence, we refer to the front propagation at this limit as *diffusion limited*. On the other hand, if $\mathcal{K} \ll 1$, the release of liquid lingers while liquid B migrates at a faster rate. Hence, we refer to front propagation at this limit as *dissolution limited*.

Now, to illustrate the effect of elasticity on the long-timescale behavior, we consider an example scenario. The time-evolution of a system following quenching from 40°C to 25°C is portrayed in Fig. 4 by the volume fractions on the stiff side at various times. Curves are obtained using a representative set of model parameters ($D, \mathcal{K}, E_{soft}, E_{stiff}, \Gamma, v_m, \phi_{sat}, n_d, \alpha, r_0$). Fig. 4(a) shows that the matrix volume fraction displays a characteristic diffusive profile, governed by the smaller volume fraction on the soft side. The source (Fig. 4(b)) is activated to replenish the matrix until it is depleted, and the front appears to propagate into the stiff side (i.e along the positive x direction). For smaller values of \mathcal{K} , source is slower in giving up liquid B resulting in dissolution-limited front propagation. Fig. 4(c) illustrates the origin of \mathcal{K} -based differences by looking at the boundary where the driving force vanishes in the (ϕ_B, ϕ_D) plane. This curve represents the locus of quasi-equilibrium states given by $s(\phi_B, \phi_D) = 0$, for a fixed stiffness. For $\mathcal{K} = 1$, the system quickly reaches the zero driving force, implying that the source continually gives up more liquid to maintain equilibrium with the depleting matrix. In contrast, for $\mathcal{K} = 10^{-2}$, the source response is much slower and is not able to achieve a rapid equilibrium with the matrix, thus making the dissolution of the droplets as the process that controls the front propagation.

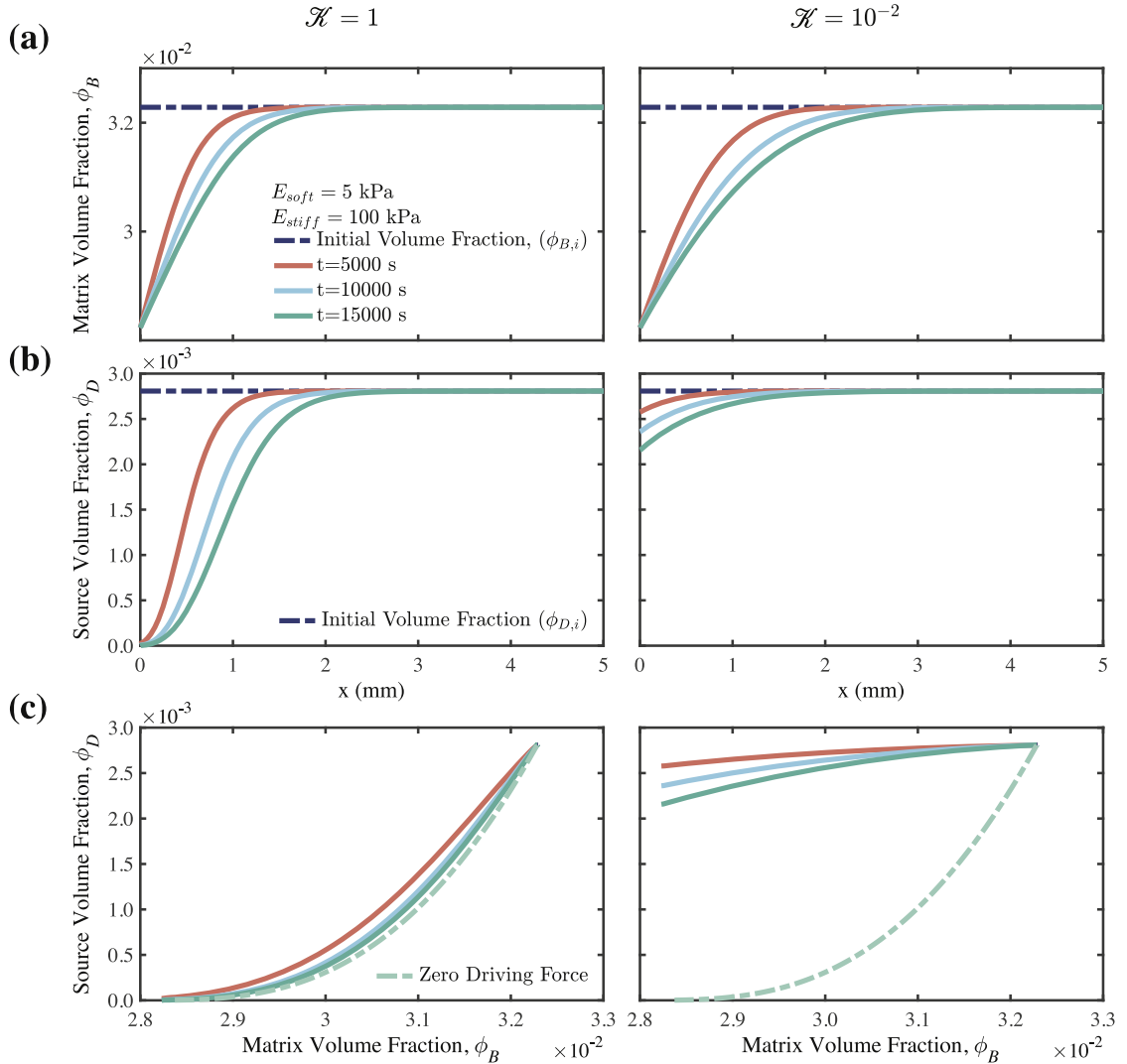


Fig. 4. Front Propagation. Predictions are shown for long range migration of liquid *B* from a stiff polymer ($E_{stiff} = 100$ kPa) to a soft polymer ($E_{soft} = 5$ kPa), both with strain-stiffening coefficient $n = 0.9$. The model parameters are: $D = 5 \times 10^{-11} \text{ m}^2\text{s}^{-1}$, $L = 10^{-3} \text{ m}$, $\Gamma = 10^{-3} \text{ Nm}^{-1}$, $v_m = 10^{-27} \text{ m}^3$, $\phi_{sat} = 0.0005T[^\circ\text{C}] + 0.015$, $n_d = \alpha E$, $\alpha = 2 \times 10^7 \text{ N}^{-1}\text{m}^{-1}$ and $r_0 = 0.1 \text{ }\mu\text{m}$. Both sides were saturated at 40°C and then quenched to 25°C , which decides their initial conditions. Results are shown for $\mathcal{K} = 1, 10^{-2}$. (a) Volume fraction of liquid *B* in the matrix is shown for the stiff side, with the interface at $x = 0$. The liquid *B* migrates from stiff to soft side. (b) The source volume fraction, representative of the size of the droplets, visually represents a dissolution front progressing further into the stiff side over time. (c) The system approaches zero driving force at different rates based on \mathcal{K} .

It is now possible to examine the effect of model parameters on the propagation of the front. We define the *location* of the front as the x coordinate where the source volume fraction is half of its initial value. The front starts propagating from $x = 0$ in the positive x direction; its location for different values of \mathcal{K} is shown in Fig. 5. The location of the front follows $x = At^{1/2}$ for $\mathcal{K} \geq 1$. This behavior is typical of diffusive fronts and thus, the front location is expected to follow this in the diffusion limited propagation. For $\mathcal{K} \ll 1$, the location trend approaches the $t^{1/2}$ limit in long-time behavior, but shows deviations initially. In particular, lower dissolution numbers lead to an increasing delay before the source volume fraction drops below half of its initial value, leading to a perceived jump in the movement of the front.

The choice of stiffnesses is an important factor that governs the speed, or equivalently, the coefficient A . Results for the example case with representative values of model parameters ($D, \mathcal{K}, E_{soft}, E_{stiff}, \Gamma, v_m, \phi_{sat}, n_d, \alpha, r_0$) are shown in Fig. 6. Increasing the stiffness of both the soft and the stiff sides while keeping fixed their difference ($\Delta E = E_{stiff} - E_{soft}$), changes the speed non-monotonically as seen in Fig. 6(a). This challenges the current understanding that the front speed only depends on the stiffness difference. The front speed, in fact, also depends on the individual stiffness of either side and this may lead to a scenario where the front speeds approach the same value regardless of the ΔE . Fig. 6(b) shows that if E_{soft} is held constant, the speed increases nonlinearly with increasing ΔE .

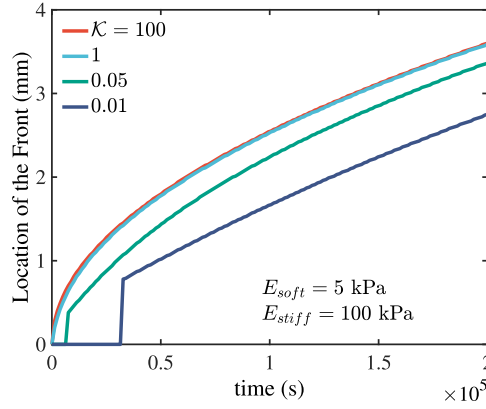


Fig. 5. Front Location. Model predictions are shown for the location of the front. The model parameters are: $D = 5 \times 10^{-11} \text{ m}^2\text{s}^{-1}$, $\Gamma = 10^{-3} \text{ Nm}^{-1}$, $v_m = 10^{-27} \text{ m}^3$, $\phi_{sat} = 0.0005T[^\circ\text{C}] + 0.015$, $n_d = \alpha E$, $\alpha = 2 \times 10^7 \text{ N}^{-1}\text{m}^{-1}$ and $r_0 = 0.1 \text{ }\mu\text{m}$. Both sides were saturated at 40°C and then quenched to 25°C , which decides their initial conditions.

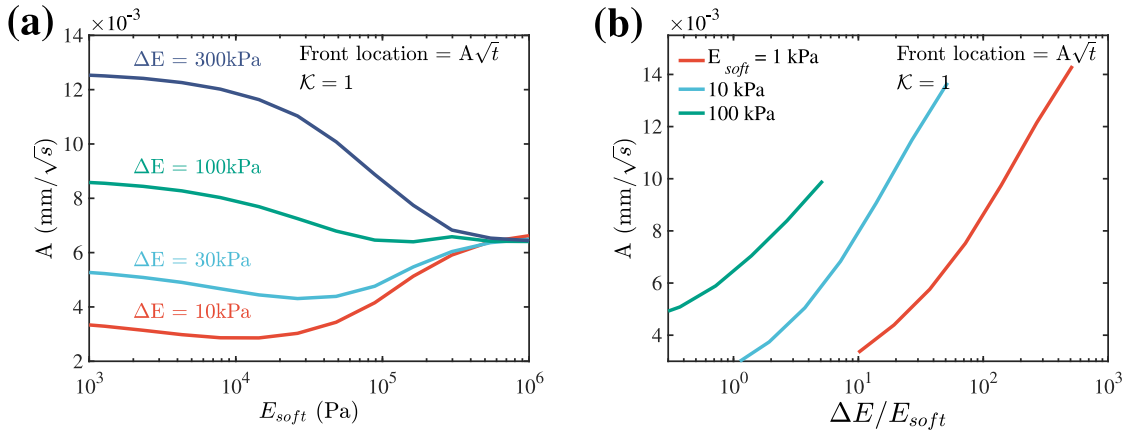


Fig. 6. Elastic Properties Have a Nonlinear Effect on Front Speed. Model predictions are shown for the parameter A that determines the front speed. The model parameters are: $D = 5 \times 10^{-11} \text{ m}^2\text{s}^{-1}$, $\Gamma = 10^{-3} \text{ Nm}^{-1}$, $v_m = 10^{-27} \text{ m}^3$, $\phi_{sat} = 0.0005T[^\circ\text{C}] + 0.015$, $n_d = \alpha E$, $\alpha = 2 \times 10^7 \text{ N}^{-1}\text{m}^{-1}$ and $r_0 = 0.1 \text{ }\mu\text{m}$. Both sides were saturated at 40°C and then quenched to 25°C , which decides their initial conditions. The speed of the 50%-depletion front (a) changes non-monotonically with stiffness of the soft-side, while keeping ΔE fixed, (b) increases monotonically with ΔE , while keeping the soft-side stiffness constant.

3. Experimental validation

We carry out the validation of our model by comparison with the experimental results reported in the literature. We use a set of parameters ($v_m, N_A, \phi_{sat}, \Gamma, n_d$) reported in [Style et al. \(2018\)](#) and [Rosowski et al. \(2020a\)](#), along with $r_c = 1 \text{ }\mu\text{m}$. To examine the sensitivities, model predictions are obtained using two different values of the stress-free cavity size ($r_0 = 1 \text{ }\mu\text{m}$ and $r_0 = 1 \text{ nm}$), and strain stiffening ($n = 0.9$ and $n = 1$). Although only the linear elastic modulus was reported in [Rosowski et al. \(2020a\)](#), our choice of $n = 0.9$ (moderate strain-stiffening) for the Mooney-Rivlin constitutive model is motivated by the recent measurements in a similar material system ([Raayai-Ardakani and Cohen, 2019](#)).

The critical temperature, T_c , and equilibrium droplet size are shown in [Fig. 7](#) for different stiffnesses. Good agreement between the experimental results ([Rosowski et al., 2020a; Style et al., 2018](#)) and model prediction is observed for $r_0 = 0.1 \text{ }\mu\text{m}$ with $n = 0.9$ (red curve). Some discrepancy is observed in prediction of droplet size in the soft-stiffness range ([Fig. 7\(b\)](#)) and could be explained by the reported polydisperse droplet size in the low-stiffness regime.

If r_0 is chosen as the pore size of the polymer ($r_0 \sim 1 \text{ nm}$), the strain-stiffening material requires a much deeper quench and underpredicts the droplet size when compared to experiments. This reinforces the idea that pore size of the polymer is not the appropriate choice for r_0 .

We note that for a neo-hookean material ($n = 1$) undergoing large stretches, the internal pressure approaches an asymptotic value of $p = 5E/6$ (as seen from [Eq. \(B.4\)](#) in Appendix B, with $\lambda_a = r/r_0 \gg 1$). Thus, the model predictions are insensitive to the choice of r_0 . As shown in [Fig. 7\(a\)](#), if a neo-Hookean response is assumed, it will lead to a crude overestimation of the critical temperature (notice that deviations are larger than they appear due to the log-scale representation). Further, neo-Hookean model is, typically, not accurate for large stretches. Finally, the curves in [Fig. 7](#) suggest that progressive damage has a negligible role; accounting for increasing values of r_0 in the softer range, where the droplets are larger, would have

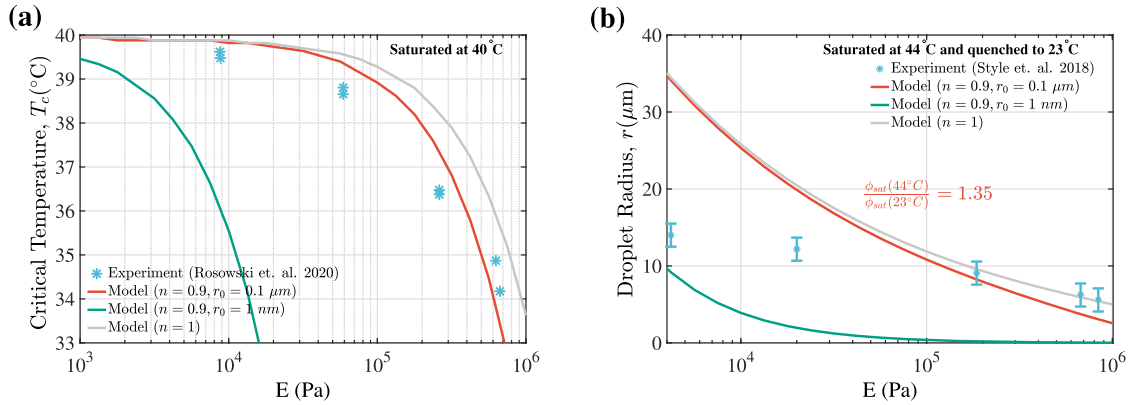


Fig. 7. Comparison of Model Predictions with Experiments Model predictions are compared with experimental results (Rosowski et al., 2020a; Style et al., 2018) with the following model parameters: $v_m = 3.7 \times 10^{-28} \text{ m}^3$, $N_A = 1$, $\phi_{sat} = 0.0004677[^\circ\text{C}] + 0.01728$, $\Gamma = 4 \times 10^{-3} \text{ Nm}^{-1}$, $n_d = \alpha E$ and $\alpha = 1.4 \times 10^7 \text{ N}^{-1} \text{ m}^{-1}$. The saturation temperatures are indicated on the figures. (a) Critical temperature prediction shows good agreement with experiments for a moderate strain-stiffening elastic response ($n = 0.9$) with $r_0 = 0.1 \mu\text{m}$ (b) Model predictions show good agreement for high stiffness and overprediction for smaller stiffness, for a moderate strain-stiffening elastic response ($n = 0.9$) with $r_0 = 0.1 \mu\text{m}$.

a negligible effect in the current scenario, as seen from the upper bound limit of the neo-Hookean model, and in general, may increase the deviations between theory and experiments.

For the front propagation at the longer timescale, while there is not enough experimental data to quantitatively compare with model predictions, we find qualitative agreement between the limited experimental data and model predictions for $\mathcal{K} = 1$. Further experimental investigation of front speeds with varying elastic properties is necessary to fully understand the nonlinear elastic effects and the various regimes of front propagation.

4. Discussion and conclusions

In this work, we study the effect of elasticity on the phase separation of binary liquid mixtures and the resulting long-range species migration in heterogeneous materials. A thermodynamically-consistent theoretical model that captures the influence of nonlinear elastic properties on both the formation of precipitates and the subsequent process of their dissolution across a propagating front, is proposed. To our knowledge, no systematic theoretical study of elastic effects on the formation and dynamics of *liquid precipitates* in soft nonlinear elastic solids has been carried out till date.

In typical liquid-liquid phase separation, once the liquid droplets cross the energy barrier imposed by surface energy, they can continue to grow. However, in the presence of an elastic matrix, the droplet has to work against the elastic resisting force to activate large deformations, which increases both the nucleation barrier as well as the energetic cost of growing the droplet. Our model reveals the contribution of both surface tension and elastic properties to the nucleation barrier and the quasi-equilibrium separated state. The equilibrium droplet size is determined by minimization of free energy and is shown to scale with the supersaturation. Stiffer and strain-stiffening materials show smaller droplet sizes due to their higher solubility of the minority component. We show that these effects follow nonlinear trends. The analysis assumes that the short-timescale process of phase separation is well separated from the long-timescale process of species migration; this is ensured by requiring a rapid quench.

The long-time dynamics that can arise in presence of material heterogeneity are studied through an illustrative example of a graded sample comprising a stiff and a soft polymer joined together. For this example, diffusion of the minority component is affected by a concentration mismatch, and leads to formation of a dissolution front. A thermodynamic argument is employed to model the chemo-mechanically coupled kinetics of dissolution, which are found to be governed by the dimensionless dissolution number (\mathcal{K}). Distinct regimes of *diffusion dominated* and *dissolution dominated* front propagation are shown to emerge, for different ranges of \mathcal{K} . Elasticity is shown to govern the speed of the front by controlling the quasi-equilibrated matrix volume fraction of the minority component on either side of the graded polymer. If the droplet volume is large, the source (i.e. droplet content) is large, thereby taking longer to deplete it and vice versa. Accordingly, the front moves faster in stiffer materials where the higher solubility implies smaller droplet volume. Since the volume fraction of the minority component depends nonlinearly on the stiffness, the speed of the front also shows a nonlinear trend. In fact, it not only exhibits a non-monotonic dependence on the stiffness difference between the soft and stiff sides (ΔE), but is also shown to depend separately on the individual stiffnesses.

While in this paper our focus is on the effect of elasticity on the process of phase separation, a number of other variables can play similar role in controlling the solubility and migration of species. For instance, local changes in temperature can affect the solubility and the Flory interaction parameter (χ), which affects the droplet size at the short timescale and, in turn, dictates the long timescale migration. In this way it is possible to reverse the Ostwald Ripening process in order to grow smaller droplets at the cost of larger ones, as observed recently (Rosowski et al., 2020b). Dissimilar strain-stiffening

behavior can also significantly affect the stresses in the matrix, which directly affects both the short- and long-timescale behavior. As an example, a material with higher strain-stiffening will show smaller droplet size when compared to another material with the same stiffness, leading to differences in long-time behavior. Application of external stresses on the system can also have a similar effect. The model presented here can provide guidance to quantitatively determine the appropriate combination of these factors to achieve a desired outcome.

Finally, this work highlights the importance of elasticity as a potential regulating mechanism for controlling solubility and phase-separation in various physical settings. Tuning the elastic properties of the matrix material can impart control over the stable droplet distribution for industrial applications, it can drive the formation of membraneless organelles in biological settings, and can affect the transport of potent greenhouse gases in soil. Although these systems may differ in lengthscale and diffusion properties, given the elastic properties, their long-time evolution can be qualitatively predicted based on the value of their dissolution number. Future work should extend to more complex heterogeneous settings, and should provide additional insights into the early stages of droplet nucleation and growth, before continuum scale is attained.

Declaration of Competing Interest

There are no conflicts of interest to declare.

CRediT authorship contribution statement

M. Kothari and T. Cohen conceived the mathematical models, interpreted the computational results, and wrote the paper. M. Kothari performed the numerical simulations. Both authors gave final approval for publication.

Acknowledgements

The authors would like to thank Eric R. Dufresne and Robert W. Style for introducing us to this problem. The authors would like to acknowledge helpful discussions with Prashant K. Purohit and Vaishali Garga. The authors also wish to acknowledge the support of the Office of Naval Research, United States of America and Dr. Timothy B. Bentley, Program Manager, under award number N00014-20-1-2561.

Appendix A. Flory interaction parameter

Upon soaking the polymer in a bath of liquid B , it is saturated and reaches equilibrium. Since the saturated state is a homogeneously mixed state, $V_D = 0$ and $V = V_M$. The change in free energy upon soaking the polymer in liquid B is given as,

$$\Delta G_{mix} = V \frac{kT}{v_m} \left\{ \frac{\phi_A}{N_A} \ln \phi_A + \phi_B \ln \phi_B + \chi(T) \phi_B (1 - \phi_B) \right\} \quad (\text{A.1})$$

$$= \frac{kT}{v_m} \left\{ \frac{V_A}{N_A} \ln \frac{V_A}{V_0 + V_B} + V_B \ln \frac{V_B}{V_0 + V_B} + \chi(T) V_B \left(1 - \frac{V_B}{V_0 + V_B} \right) \right\}. \quad (\text{A.2})$$

The saturation volume fraction ϕ_{sat} of liquid B is obtained by minimizing ΔG_{mix} with V_B ,

$$\left. \frac{\partial \Delta G_{mix}}{\partial V_B} \right|_{\phi_B = \phi_{sat}} = 0, \quad (\text{A.3})$$

which gives,

$$\chi = - \frac{\log \phi_{sat} + (1 - \phi_{sat})(1 - 1/N_A)}{(1 - \phi_{sat})^2}. \quad (\text{A.4})$$

Appendix B. Expansion of a droplet in a Mooney-Rivlin solid

The total elastic work done in expanding a spherically symmetric droplet from a stress-free state of radius A to a final size of radius a , under the action of internal pressure, p , is calculated here assuming an unbounded and incompressible surrounding medium.

The pressure-stretch relationship can then be obtained as in [Raayai-Ardakani et al. \(2019\)](#),

$$p = \int_{\lambda_a}^1 \frac{\psi'(\lambda_\theta)}{1 - \lambda_\theta^3} d\lambda_\theta \quad (\text{B.1})$$

where ψ is the strain-energy density function, specialized to the considered spherically symmetric deformation pattern, written in terms of $\lambda_\theta = r/R$, the circumferential stretch and its value at the cavity wall $\lambda_a = a/A$. Here, R and r represents the undeformed and deformed radial coordinates, respectively. The radial stretch is given by $\lambda_r = \partial r / \partial R$, which in view of the incompressibility constraint, with the azimuthal stretch $\lambda_\phi = \lambda_\theta$, specializes to $\lambda_r = \lambda_\theta^{-2}$.

In this work we consider material response modeled by the Mooney-Rivlin strain energy density, which is given as,

$$\psi = \frac{E}{6}(n(I_1 - 3) + (1 - n)(I_2 - 3)), \quad (\text{B.2})$$

where E is the linear elastic modulus, n is the strain-stiffening parameter, and the first and second invariants of the left Cauchy-Green tensor are

$$I_1 = \lambda_r^2 + \lambda_\theta^2 + \lambda_\phi^2, \quad I_2 = \lambda_r^2\lambda_\theta^2 + \lambda_\theta^2\lambda_\phi^2 + \lambda_\phi^2\lambda_r^2. \quad (\text{B.3})$$

By combining equations (B.1–B.3) we write the cavity pressure as

$$p(\lambda_a) = nE\left(\frac{5}{6} - \frac{2}{3\lambda_a} - \frac{1}{6\lambda_a^4}\right) + (1 - n)E\left(\frac{2\lambda_a}{3} - \frac{1}{3} - \frac{1}{3\lambda_a^2}\right). \quad (\text{B.4})$$

The pressure-stretch relationship can be readily used to calculate the work done in expanding the cavity from stress-free radius A to final radius a ,

$$U(\lambda_a) = 4\pi A^3 \int_1^{\lambda_a} p(\lambda)\lambda^2 d\lambda \quad (\text{B.5})$$

$$= \frac{4\pi}{3} a^3 nE\left(\frac{5}{6} - \frac{1}{\lambda_a} - \frac{1}{3\lambda_a^3} + \frac{1}{2\lambda_a^4}\right) + \frac{4\pi}{3} a^3 (1 - n)E\left(\frac{\lambda_a}{2} - \frac{1}{3} - \frac{1}{\lambda_a^2} + \frac{5}{6\lambda_a^3}\right). \quad (\text{B.6})$$

The energy density per droplet is then given as,

$$W(a) = \frac{U(\lambda_a)}{4\pi a^3/3} = nE\left(\frac{5}{6} - \frac{1}{\lambda_a} - \frac{1}{3\lambda_a^3} + \frac{1}{2\lambda_a^4}\right) + (1 - n)E\left(\frac{\lambda_a}{2} - \frac{1}{3} - \frac{1}{\lambda_a^2} + \frac{5}{6\lambda_a^3}\right). \quad (\text{B.7})$$

Appendix C. Equilibrium Droplet Size

We consider the crosslinked polymer saturated with liquid B to a volume fraction $\phi_{sat}(T_1)$ at a temperature T_1 . The assembly is then quenched to a lower temperature T . Since we consider a closed system during quenching, the total volume of liquid B is the same as when the system was saturated, i.e. $V_B + V_D = \phi_{sat}(T_1)V$. Now, the total free energy change upon phase separation can be given as,

$$\Delta G = \frac{kT}{v_m} \left\{ \frac{V_A}{N_A} \ln \frac{V_A}{V_0 + V_B} + V_B \ln \frac{V_B}{V_0 + V_B} + \chi(T)V_B \left(1 - \frac{V_B}{V_0 + V_B}\right) \right\} + V_D \left\{ W(r) + \frac{3\Gamma}{r} \right\}. \quad (\text{C.1})$$

The equilibrium equation,

$$\frac{d\Delta G}{dV_B} = 0, \quad (\text{C.2})$$

gives the following implicit relation for the equilibrium droplet size,

$$\ln \phi_B + (1 - \phi_B)(1 - 1/N_A) + \chi(1 - \phi_B)^2 = \frac{v_m}{kT} \left(\frac{2\Gamma}{r} + W(r) + \frac{r}{3} W'(r) \right), \quad (\text{C.3})$$

where ϕ_B is related to the droplet size, r , by the mass conservation constraint (Eq. (6) in the main text).

References

- Algar, C.K., Boudreau, B.P., 2010. Stability of bubbles in a linear elastic medium: implications for bubble growth in marine sediments. *J. Geophys. Res. Earth Surface* 115 (F3).
- Brangwynne, C.P., Eckmann, C.R., Courson, D.S., Rybarska, A., Hoeghe, C., Gharakhani, J., Jülicher, F., Hyman, A.A., 2009. Germline P granules are liquid droplets that localize by controlled dissolution/condensation. *Science* 324 (5935), 1729–1732.
- Briber, R.M., Bauer, B.J., 1988. Effect of crosslinks on the phase separation behavior of a miscible polymer blend. *Macromolecules* 21 (11), 3296–3303.
- Doi, M., Miyazaki, T., Wakatsuki, T., 1985. The effects of elastic interaction energy on the $\gamma\dot{U}$ precipitate morphology of continuously cooled nickel-base alloys. *Mater. Sci. Eng.* 74 (2), 139–145.
- Fratzl, P., Penrose, O., Leibowitz, J.L., 1999. Modeling of phase separation in alloys with coherent elastic misfit. *J. Stat. Phys.* 95 (5–6), 1429–1503.
- de Gennes, P.-G., 1979. Effect of cross-links on a mixture of polymers. *J. Phys. Lett.* 40 (4), 69–72.
- Gent, A., 2001. Engineering with rubber: how to design rubber components.
- Gent, A.N., Tompkins, D.A., 1969. Surface energy effects for small holes or particles in elastomers. *J. Polym. Sci. Part A-2 Polym. Phys.* 7 (9), 1483–1487.
- Johnson, B.D., Boudreau, B.P., Gardiner, B.S., Maass, R., 2002. Mechanical response of sediments to bubble growth. *Mar. Geol.* 187 (3–4), 347–363.
- Karpov, S.Y., 1998. Suppression of phase separation in InGaN due to elastic strain. *Mater. Res. Soc. Internet J. Nitride Semicond. Res.* 3.
- Kim, J.Y., Liu, Z., Weon, B.M., Cohen, T., Hui, C.-Y., Dufresne, E.R., Style, R.W., 2020. Extreme cavity expansion in soft solids: damage without fracture. *Sci. Adv.* 6 (13), eaaz0418.
- Kothari, M., Niu, S., Srivastava, V., 2019. A thermo-mechanically coupled finite strain model for phase-transitioning austenitic steels in ambient to cryogenic temperature range. *J. Mech. Phys. Solids* 133, 103729.
- Lee, C.F., Brangwynne, C.P., Gharakhani, J., Hyman, A.A., Jülicher, F., 2013. Spatial organization of the cell cytoplasm by position-dependent phase separation. *Phys. Rev. Lett.* 111 (8), 088101.
- Liu, L., De Kock, T., Wilkinson, J., Cnudde, V., Xiao, S., Buchmann, C., Uteau, D., Peth, S., Lorke, A., 2018. Methane bubble growth and migration in aquatic sediments observed by x-ray μ CT. *Environ. Sci. Technol.* 52 (4), 2007–2015.
- Mooney, M., 1940. A theory of large elastic deformation. *J. Appl. Phys.* 11 (9), 582–592.
- Nabarro, F., 1940. The influence of elastic strain on the shape of particles segregating in an alloy. *Proc. Phys. Soc.* 52 (1), 90.

- Porter, D.A., Easterling, K.E., Sherif, M., 2009. Phase Transformations in Metals and Alloys, (revised reprint). CRC press.
- Raayai-Ardakani, S., Chen, Z., Earl, D.R., Cohen, T., 2019. Volume-controlled cavity expansion for probing of local elastic properties in soft materials. *Soft Matter* 15 (3), 381–392.
- Raayai-Ardakani, S., Cohen, T., 2019. Capturing strain stiffening using volume controlled cavity expansion. *Extreme Mech. Lett.* 31, 100536.
- Rivlin, R., 1948. Large elastic deformations of isotropic materials. I. fundamental concepts. *Philos. Trans. R. Soc. London Ser A Math. Phys. Sci.* 240 (822), 459–490.
- Rosowski, K.A., Sai, T., Vidal-Henriquez, E., Zwicker, D., Style, R.W., Dufresne, E.R., 2020. Elastic ripening and inhibition of liquid–liquid phase separation. *Nat. Phys.* 1–4.
- Rosowski, K. A., Vidal-Henriquez, E., Zwicker, D., Style, R. W., Dufresne, E. R., 2020b. Elastic stresses reverse Ostwald ripening. [arXiv:2004.05070](https://arxiv.org/abs/2004.05070).
- Saha, S., Weber, C.A., Nusch, M., Adame-Arana, O., Hoegge, C., Hein, M.Y., Osborne-Nishimura, E., Mahamid, J., Jahnel, M., Jawerth, L., et al., 2016. Polar positioning of phase-separated liquid compartments in cells regulated by an mRNA competition mechanism. *Cell* 166 (6), 1572–1584.
- Smith, T.M., Esser, B.D., Antolin, N., Carlsson, A., Williams, R., Wessman, A., Hanlon, T., Fraser, H.L., Windl, W., McComb, D.W., et al., 2016. Phase transformation strengthening of high-temperature superalloys. *Nat. Commun.* 7 (1), 1–7.
- Style, R.W., Sai, T., Fanelli, N., Ijavi, M., Smith-Mannschott, K., Xu, Q., Wilen, L.A., Dufresne, E.R., 2018. Liquid-liquid phase separation in an elastic network. *Phys. Rev. X* 8 (1), 011028.
- Tancret, F., Laigo, J., Christien, F., Le Gall, R., Furtado, J., 2018. Phase transformations in Fe–Ni–Cr heat-resistant alloys for reformer tube applications. *Mater. Sci. Technol.* 34 (11), 1333–1343.
- Vidal-Henriquez, E., Zwicker, D., 2020. Theory of droplet ripening in stiffness gradients. [arXiv:2001.11752](https://arxiv.org/abs/2001.11752).
- Weber, C.A., Lee, C.F., Jülicher, F., 2017. Droplet ripening in concentration gradients. *New J Phys* 19 (5), 053021.
- Weber, C.A., Zwicker, D., Jülicher, F., Lee, C.F., 2019. Physics of active emulsions. *Rep. Prog. Phys.* 82 (6), 064601.